MULTIMILLION ATOM SIMULATIONS AND VISUALIZATION OF HYPERVELOCITY IMPACT DAMAGE AND OXIDATION

Priya Vashishta[*], Rajiv K. Kalia, and Aiichiro Nakano
Collaboratory for Advanced Computing and Simulations
Department of Materials Science & Engineering, Department of Physics & Astronomy,
Department of Computer Science
University of Southern California, Los Angeles, CA 90089-0242
Email: (priyav, rkalia, anakano)@usc.edu

ABSTRACT

Large-scale molecular dynamics simulation involving several hundred million atoms has been performed on parallel computers to study hypervelocity impact damage of high-strength aluminum nitride ceramic, which is of great importance for the design of penetration-resistant and light-weight armors at the Army. Results reveal an atomistic mechanism of damage initiation, i.e., the phase transformation wave front acts as a source of dislocations and micro-cracks upon the arrival of an elastic rarefaction wave. Simulation has also been performed to study atomistic mechanisms of oxidation of an Al nanoparticle, which has applications in high-energy density materials. A multi-resolution and probabilistic visualization algorithm has been developed to interactively analyze massive datasets from these simulations.

1. INTRODUCTION

High-strength ceramics such as B_4C, SiC, Si_3N_4, Al_2O_3 and AlN have promising technological applications as coatings and armors, because of their outstanding properties such as high hardness and strength, while having low densities compared to metals. These ceramics are strong in compression, which allows them to effectively break impacting projectiles. However, they are brittle and weak in tension, and their efficiency can be seriously degraded by fracture, which reduces their ability to withstand subsequent impacts. Understanding microscopic mechanisms of impact damage of high-strength ceramics is thus of great importance for the design of better ceramic compound coatings and armors at the Army.

Recently, metallic nanoparticles and their composites have been considered for high energy density materials (HEDM) applications such as propellants and explosives. Burn rates of propellants and explosives can be accelerated by reducing the size of reactant particles such as Al. One main disadvantage of such nanometric reactant particles is the dead weight of oxide layers. It is thus of great importance to study atomistic mechanisms of oxidation of an Al nanoparticle.

This paper describes our 209 million-atom molecular-dynamics (MD) simulation of hypervelocity impact damage in AlN and a million-atom variable-charge molecular dynamics (VCMD) simulation of oxidation dynamics of an Al nanoparticle.

To interactively visualize large atomistic datasets from large-scale MD simulations such as described above, we have developed a scalable and portable code named Atomsviewer. The paper also describes main features of the Atomsviewer.

2. HYPERVELOCITY IMPACT OF ALUMINUM NITRIDE

We have performed 209 million-atom MD simulation to study atomistic mechanisms of damage initiation in AlN during hypervelocity impact of a projectile (Branicio, et al., 2004). The MD simulation is performed on a wurtzite crystalline AlN target with a slab shape of dimensions 150 × 150 × 100 nm in the x, y and z directions, where the z-axis parallel to the [0001] orientation of the wurtzite crystal is chosen as the impact direction. The projectile is a hexagonal cylinder of 15 nm wide and 30 nm long. The forces between atoms are calculated using our many-body interatomic potential form. The potential parameters were fitted to reproduce the elastic moduli, cohesive energy, and lattice constants. Calculated melting temperature and the wurtzite-to-rocksalt structural phase transformation (SPT) pressure are in agreement with experimental values. The energy barriers to dislocation emission, i.e., the unstable stacking fault energy and the unstable twinning energy agree within 10% and 17% to electronic structure calculations. In the simulation, the projectile hits the central point of the (0001) front surface of the target at a speed of 15 km/s.

Results show that the initially overdriven shock wave splits into an elastic wave travelling ahead of the SPT wave; the latter drives the AlN crystal from the 4-coordinated wurtzite structure to the more compact 6-coordinated rocksalt structure, as the local pressure

Report Documentation Page	*Form Approved* *OMB No. 0704-0188*

Public reporting burden for the collection of information is estimated to average 1 hour per response, including the time for reviewing instructions, searching existing data sources, gathering and maintaining the data needed, and completing and reviewing the collection of information. Send comments regarding this burden estimate or any other aspect of this collection of information, including suggestions for reducing this burden, to Washington Headquarters Services, Directorate for Information Operations and Reports, 1215 Jefferson Davis Highway, Suite 1204, Arlington VA 22202-4302. Respondents should be aware that notwithstanding any other provision of law, no person shall be subject to a penalty for failing to comply with a collection of information if it does not display a currently valid OMB control number.

1. REPORT DATE **00 DEC 2004**	2. REPORT TYPE **N/A**	3. DATES COVERED **-**	
4. TITLE AND SUBTITLE **Multimillion Atom Simulations And Visualization Of Hypervelocity Impact Damage And Oxidation**		5a. CONTRACT NUMBER	
		5b. GRANT NUMBER	
		5c. PROGRAM ELEMENT NUMBER	
6. AUTHOR(S)		5d. PROJECT NUMBER	
		5e. TASK NUMBER	
		5f. WORK UNIT NUMBER	
7. PERFORMING ORGANIZATION NAME(S) AND ADDRESS(ES) **Collaboratory for Advanced Computing and Simulations Department of Materials Science & Engineering, Department of Physics & Astronomy, Department of Computer Science University of Southern California, Los Angeles, CA 90089-0242**		8. PERFORMING ORGANIZATION REPORT NUMBER	
9. SPONSORING/MONITORING AGENCY NAME(S) AND ADDRESS(ES)		10. SPONSOR/MONITOR'S ACRONYM(S)	
		11. SPONSOR/MONITOR'S REPORT NUMBER(S)	

12. DISTRIBUTION/AVAILABILITY STATEMENT
Approved for public release, distribution unlimited

13. SUPPLEMENTARY NOTES
See also ADM001736, Proceedings for the Army Science Conference (24th) Held on 29 November - 2 December 2005 in Orlando, Florida. , The original document contains color images.

14. ABSTRACT

15. SUBJECT TERMS

16. SECURITY CLASSIFICATION OF:			17. LIMITATION OF ABSTRACT **UU**	18. NUMBER OF PAGES **6**	19a. NAME OF RESPONSIBLE PERSON
a. REPORT **unclassified**	b. ABSTRACT **unclassified**	c. THIS PAGE **unclassified**			

Standard Form 298 (Rev. 8-98)
Prescribed by ANSI Std Z39-18

reaches the transition pressure of ~20 GPa; see Fig. 1. After the splitting, the elastic wave travels at ~12 km/s, whereas the SPT wave speed drops continuously until it halts at 10 ps, as the pressure drops below the transition pressure.
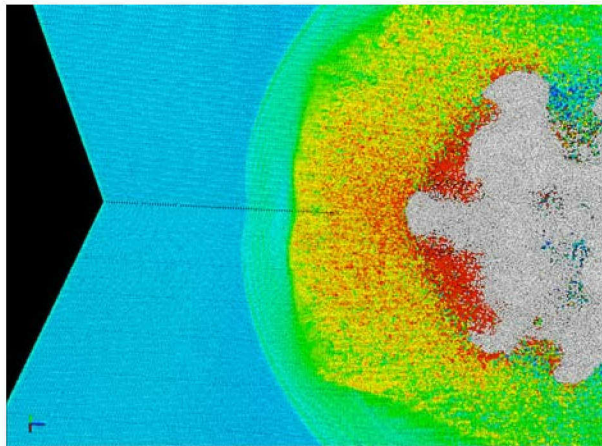
Fig. 1: MD simulation of hypervelocity impact of a projectile on a 209 million-atom AlN target. Only a 3/4 cut of the target is shown to visualize the internal pressure distribution. The figure shows the splitting of the shock wave into an elastic precursor (in light green) and a structural transformation wave (in dark green).

The SPT wave front becomes a favourable spot for stress concentration and defect generation, when it interacts with elastic waves. When the compressive wave hits the back free surface of the target, a tensile wave is generated and propagates in the reverse direction. As soon as this tensile wave reaches the wurtzite-rocksalt interface, several nanocavities start to nucleate. When the release waves from the free surface maximize the shear stress, another type of defect is generated at the wurtzite-rocksalt interface. The impact direction is aligned with the [0001] direction of the wurtzite crystal, which is perpendicular to the basal plane, i.e., the easy glide plane for dislocations. Since the planes of the highest shear stress due to localized pressure do not coincide with this basal plane, the shear stress cannot be released by nucleating dislocations. Instead, it is released through rotational plasticity, i.e., generation of a series of dislocation dipoles with opposite Burgers vectors in the basal plane, creating a kink band (crystalline region with a different crystallographic orientation from the surrounding). The kink band nucleates at the SPT wave front and develops into the defect-free wurtzite crystal. The dislocation dipoles in the basal planes forming the kink band are in fact closed dislocation loops. The dislocations lines, which form the boundary of the kink band, can move easily in the basal

plane. To maximize the rotation and stress release, the dislocations on one side of the kink band align to form a superdislocation and a high-angle tilt boundary that glides to the edge of the system.

The expansion of the target, along with the superposition of release waves, generates a growing tension in the target. This tension is concentrated at the structural defects and triggers the crack growth into the wurtzite crystal, when the Griffith criterion is reached. In our simulation, two independent mechanisms of crack nucleation and growth are identified, both rooted at the wurtzite-rocksalt interface. One mechanism is associated with the nanocavities nucleated in the wurtzite near the interface, and another associated with the high-angle tilt boundaries formed by superdislocations. In the first mechanism, cracks nucleate at the nanocavities near the interface, and propagate along the [0001] direction in mode I (opening mode). To release the maximal tangential tension due to localized expansion, the cracks cleave $(11\bar{2}0)$ planes. In the second mechanism, the cracks are nucleated along the superdislocation boundary of the kink bands. These cracks then propagate mainly in mode II (shearing mode), releasing the shear stress due to localized expansion.

The above simulation results may provide missing information in the constitutive modeling of damage for the design of high strength armors.

3. OXIDATION OF AN ALMINUM NANOPARTICLE

The dynamics of oxidation of aluminum nanoclusters (20 nm diameter) is investigated (Campbell, et al., 2004; 1999) using a parallel MD approach based on variable charge interatomic interactions (Streitz and Mintmire, 1994) that include both ionic and covalent effects.

The setup for the oxidation simulations is as follows. An fcc-crystalline Al-sphere (diameter = 200 Å) composed of 252,158 atoms and thermalized at 300 K is placed at the center of a cubic box of length 800 Å. A total of 530,720 oxygen atoms are distributed randomly outside the Al-sphere (radius 110 to 400 Å) either in the form of atomic (O_1) or molecular (O_2) oxygen at a temperature of 300 K. The oxygen density is 40 times that of the normal state (1 atm and 300 K). A spherical reflecting wall of radius 400 Å confines the entire system.

We simulated the oxidation behavior in closed conditions without heat dissipation, i.e., the simulations were performed in the microcanonical ensemble performed for both atomic (O_1) and molecular (O_2) oxygen. The time evolution of temperature and density profiles in the O_2 microcanonical simulation are calculated as a function of distance from the center of the

cluster. We observe that the energy released from Al-O bond formation leads to a dramatic increase in temperature in the surface region. Thermal energy is rapidly transported through the Al cluster, resulting in an average temperature of 1,000 K in the core of the Al cluster (the melting temperature of Al is 933 K) by 40 ps. Rapid temperature increase in the reactive region (near surface) causes nanocluster to explode. Due to the increase in temperature, the density of aluminum atoms in the surface region drops and the cluster boundary increases to around 110 Å by 30 ps. Oxygen atoms rapidly diffuse into the Al cluster, reaching a radius of 80 Å during the first 30 ps. The peak oxygen density increases rapidly during the first 30 ps and then saturates by 40 ps.

The rate of temperature increase at the nanocluster surface in the O_1 microcanonical simulation is 30% higher than that of the O_2 case. This difference is attributed to the energy required to dissociate the O_2 molecules before Al-O bonding occurs. Correspondingly, we observe that the rate of increase of the oxide layer thickness for the O_1 simulation is 13% larger than that of the O_2 simulation. The oxide thickness as a function of simulation time was calculated for both the O_1 and O_2 cases. Thickness of the oxide region grows linearly with time without saturation during the simulation for both atomic (O_1) and molecular (O_2) oxygen cases. By 50 ps the thickness and temperature of the oxide region are 35 Å and 2500 K, respectively. In addition, the saturation density of oxygen in the nanocluster surface region for the O_1 simulation is 9% lower than that of the O_2 simulation.

Figure 2 shows the evolution of oxidation in a small slice (150 Å × 150 Å × 8 Å) of the O_2 microcanonical system at various times during the simulation. The charge transfer is localized to the surface region where the Al-O bonding occurs. Energy released from Al-O bond formation is rapidly transported through the cluster resulting in disordering of the Al crystal. Disordering of the Al crystal begins at the surface and moves rapidly inward as the temperature increases, resulting in an outward expansion of the oxide region. By 40 ps the thickness of the oxide scale is 22 Å and the temperature in the oxide region is 2,000 K. Subsequently, we observe the ejection of small Al_xO_y fragments from the nanocluster surface, indicating that the nanocluster is exploding. This behavior under closed conditions has also been observed experimentally. Similar behavior is observed in the O_1 microcanonical simulation, except that the O_2 dissociation energy lowers the rate of temperature increase at the nanocluster surface by 30%.
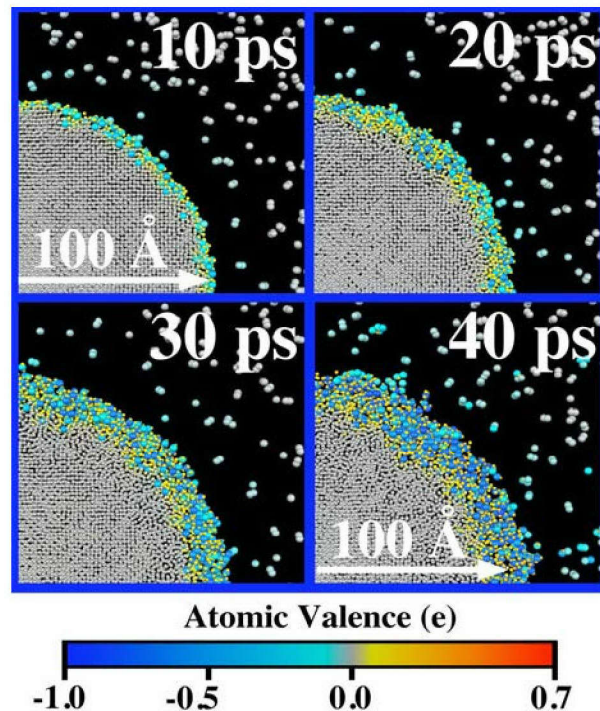

Fig. 2: Snapshots of a small slice (150 Å × 150 Å × 8 Å) of the O_2 microcanonical system at various times during the simulation. The larger spheres correspond to oxygen and smaller spheres to aluminum; color represents the sign and magnitude of the charge on an atom.

We have analyzed the evolution of local stresses during the oxidation process. The local stresses were calculated by subdividing the system into cells of length 10 Å and averaging the virial stress in each cell over 1 ps intervals. We observe large transient stress gradients followed by equilibration as the oxidation progresses. Initially, the surface region is tensile, while the inner region of the cluster is at zero pressure. We attribute the tensile stress in the surface region to the strong Coulomb forces created by the charge transfer between the surface Al atoms and the incoming O atoms. Heat transfer from the surface to the inner region then causes the pressure in the inner region to become compressive. Subsequently, the pressure differences between the surface and interior regions equilibrate.

The local stress regions are further examined by separating the contributions from the electrostatic and non-electrostatic forces. Figure 3 shows the electrostatic and non-electrostatic force contributions to the local pressure after 100 ps. It can be seen from Fig. 3(a) that the attractive Coulomb force between aluminum and oxygen contributes a large negative pressure localized in the oxide. The electrostatic pressure contribution increases in magnitude toward the middle of the oxide

where charge transfer is the highest. The large attractive forces are partially offset by steric repulsion which gives rise to a positive non-electrostatic contribution to the local pressure in the oxide, see Fig. 3(b). Analysis of local stresses reveals large stress gradients throughout the nanocluster with the oxide largely under negative pressure and the metal core under positive pressure. Local pressures range between -1 and 1 GPa. The local stresses were calculated by averaging the atomic virial in 6 Å voxels over a 1 ps interval.
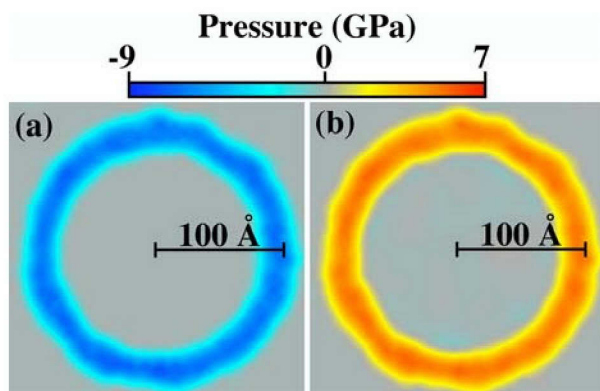

Fig. 3: (a) Electrostatic and (b) non-electrostatic contributions to the local pressure in the nanocluster after 100 ps of simulation time.

In addition to the microcanonical simulations we have investigated the oxidation process in the O_2 environment in the canonical ensemble. In the constant-temperature simulations, oxide depth grows linearly in time until ~ 30 ps, followed by saturation behavior of oxide depth as a function of time. A passivating stable amorphous oxide layer of thickness ~ 40 Å is formed after 466 ps, which is in good agreement with experiments. The average mass density in the oxide scale region is 75% of the bulk alumina density. Evolution of structural correlation in the oxide is analyzed through radial distribution and bond-angles. Through detailed analyses of the trajectories of O atoms and their formation of OAl_n structures, we propose a novel three-step process of oxidative percolation that explains deceleration of oxide growth of the nanoparticle in the canonical simulation.

4. VISUALIZATION OF MASSIVE ATOMISTIC DATA

The Atomsviewer code uses a hierarchical view frustum-culling algorithm based on the octree data structure to efficiently remove atoms outside of the user's field-of-view, i.e., view furstum culling (Sharma et al., 2004; 2003). To achieve interactive speed and scalability for view frustum culling, spatially close atoms are clustered to provide a convenient abstraction. The clustering of

atoms is performed hierarchically, using an octree data structure, see Fig. 4. An octree is a three-dimensional extension of a binary search tree, generated by recursively subdividing the three-dimensional space into smaller subregions. Each octree node thus becomes an abstraction of the atoms contained in its subspace, and we can transform the process of extracting atoms to a process of extracting regions that lie in the frustum. This transformation improves the system performance as follows. The total computation time is a sum of the time taken in culling and the time taken to render the resulting reduced set of atoms. For a typical visualization the number of rendered atoms is nearly independent of the user's viewpoint. The culling time however scales linearly with the total number of atoms, and with the octree abstraction, the computational complexity is reduced from $O(N)$ to $O(\log (N/m))$, where m is the number of atoms mapped to an octree node. The number m determines the number of subdivisions (or the depth of the octree), and it is empirically set to ~500. This number comes from a trade-off between the quality of frustum approximation, and the computation time. A larger depth implies smaller regions and therefore a more accurate representation of the frustum, but with the penalty of greater computation. Our tests involving million-to-billion atom datasets show no significant visual gains with a granularity that is finer than 500 atoms/region.
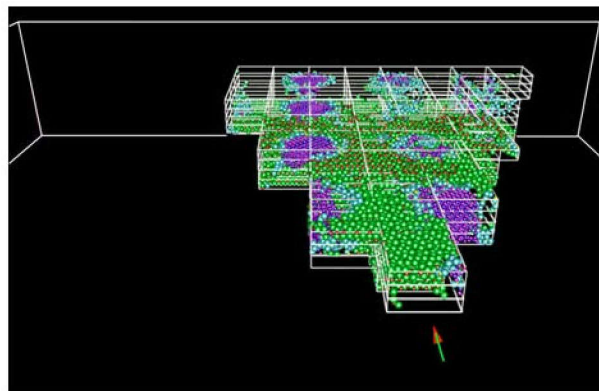
Fig. 4: Illustration of an octree data structure for visibility culling. Octree cells (bounded by white lines) dynamically approximate the current visible region (the position and viewing direction of the viewer is represented by the arrow). Only the visible atoms are processed for rendering, as demonstrated in the figure.

Probabilistic and depth-based occlusion-culling algorithms then select atoms, which have a high probability of being visible. After view frustum culling, we have a list of regions that completely occupy the view frustum. We can refine this selection by repeating

the frustum culling on atoms of those regions that lie on the boundary of the view frustum. However this test is redundant if a sufficient octree depth is taken. There are however many atoms that are in the view frustum that will be completely hidden from the viewer because of other atoms that are closer to the viewer. To remove these atoms we begin occlusion culling. In this process we sort all visible regions in an increasing order of distance from the viewer. If atoms are uniformly distributed across regions, a region that is closer to the viewer's position will contain more visible atoms than one that is further away. This is because the atoms in the nearer region will probably occlude many of the atoms in the farther region. Thus we calculate the visibility (the fraction of atoms that are probably seen by the user) of an octree region from the recurrence relation,

$$v_c = (1 - D_c)v_{c-1},$$

where v_c is the visibility of the c-th octree region and D_c is the normalized density of atoms in the c-th octree region. The 0-th octree region is the one closest to the viewer. The leaf octree regions are traversed using a line-drawing algorithm, and the visibility of each cell is calculated using the above equation. In addition to being used in billion-atom datasets, this technique is useful when the viewer is moving. The probabilistic occlusion culling decimates atoms with probability 1 - v_c, with typically a few percent pixel loss. This loss is acceptable since the user is navigating and not observing the scene. Computationally, this technique is inexpensive since visibility is assigned to octree regions and not the actual atoms.

Finally, a multiresolution algorithm is used to render the selected subset of visible atoms as spheres at varying levels of detail. The resolution of the sphere is calculated from an exponential function of distance of the atom from the viewer.

Atomsviewer is written in C++ and OpenGL, and it has been tested on a number of architectures including Windows, Macintosh, Linux, and SGI. The Atomsviewer program accepts the user position and orientation, and feeds this information to the Data Extraction Module (DEM). The DEM traverses the data file and extracts spatial clusters that fit in the user's field-of-view. These clusters are then passed through user defined coarse and fine grain filters that refine the data. This data is then filtered in the Occlusion Culling Module (OCM) to remove those atoms that are hidden from the viewer on account of other atoms occluding them. Finally the Graphic Modules (GM) render the atoms as spheres of varying size and resolution. The user can also capture the rendered scene as a snapshot or a series of time-stamped snapshots to make a movie.

Atomsviewer has been used to visualize tens of millions of atoms on a standard desktop computer and, in its parallel version, up to a billion atoms, by Army scientists. To achieve scalability, Atomsviewer is distributed over i) a cluster of PCs that executes a parallelized version of the hierarchical view frustum culling and the probabilistic occlusion culling and ii) a graphics workstation that renders the remaining atoms. We have used Atomsviewer to render a billion-atom dataset on a dual processor SGI Onyx2 with an InfiniteReality2 graphics pipeline connected to a four-node PC cluster, see Fig. 5.
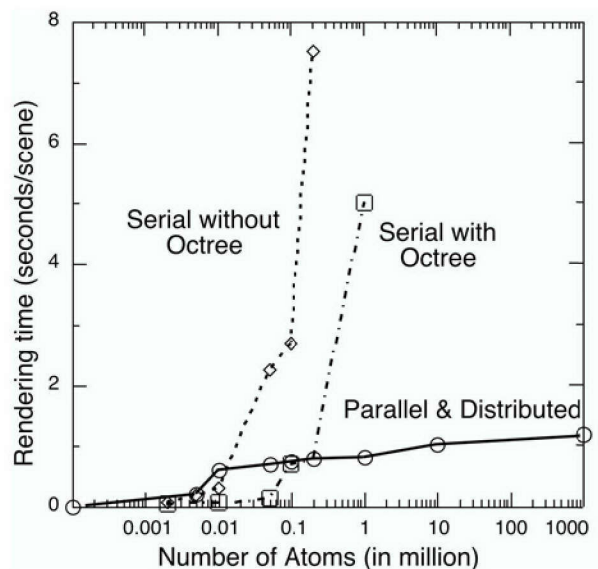
Fig. 5: **Rendering time per scene as a function of the number of atoms for the parallel and distributed Atomsviewer is compared with those for the serial Atomsviewer with and without the octree enhancement.**

5. CONCLUSION

The atomistic research efforts on hypervelocity impact damage and penetration in high-strength ceramics, as well as on oxidation dynamics in high energy density materials, will complement the continuum simulation work at the Army High Performance Computing and Research Center, and it will be essential for the design of modern lightweight armor systems for personnel, vehicles, and aircrafts, as well as propellants and explosives, for the Army and DoD.

ACKNOWLEDGEMENTS

REFERENCES

[1] Branicio, P. S., Kalia, R. K., Nakano, A. and Vashishta, P., 2004: Shock induced plasticity and brittle cracks during structural transformation in AlN, in preparation.

[2] Campbell, T. J., Aral, G., Ogata, S., Kalia, R. K., Nakano, A. and Vashishta, 2004: Oxidation of aluminum nanoclusters, *Phys. Rev. B*, to be published.

[3] Campbell, T. J., Kalia, R. K., Nakano, A., Vashishta, Ogata, S., and Rodgers, S., 1999: Dynamics of oxidation of aluminum nanoclusters using variable charge molecular-dynamics simulations on parallel computers, *Phys. Rev. Lett.* **80**, 4866-4869.

[4] Streitz, F. H. and Mintmire, J. W., 1994: Electrostatic potentials for metal-oxide surfaces and interfaces. *Phys. Rev. B* **50**, 11996.

[5] Sharma, A., Nakano, A., Kalia, and R. K., Vashishta, 2004: Scalable and portable visualization of large atomistic datasets, *Comput. Phys. Commun.*, in press.

[6] Sharma, A., Nakano, A., Kalia, R. K., Vashishta, P., Kodiyalam, S., Miller, P., Zhao, W., Liu, X. Campbell, T. J., and Haas, A., 2003: *Presence: Teleoperators and Virtual Environments* **12**, 85-95.